The Astrophysical Journal, 609:977–987, 2004 July 10

LONG-TERM SPECTRAL AND TIMING BEHAVIOR OF THE BLACK HOLE CANDIDATE XTE J1908+094

Ersin Göğüş,[1,2] Mark H. Finger,[2,3] Chryssa Kouveliotou,[3,4] Peter M. Woods,[2,3] Sandeep K. Patel,[3,5] Michael Rupen,[6] Jean H. Swank,[7] Craig B. Markwardt,[7] and Michiel van der Klis[8]

Received 2003 November 19; accepted 2004 March 23

ABSTRACT

We present the long-term X-ray light curves and detailed spectral and timing analyses of XTE J1908+094 using the *Rossi X-Ray Timing Explorer* Proportional Counter Array observations covering two outbursts in 2002 and early 2003. At the onset of the first outburst, the source was found in a spectrally low/hard state lasting for ~40 days, followed by a 3 day long transition to the high/soft state. The source flux (in 2–10 keV) reached ~100 mcrab on 2002 April 6, then decayed rapidly. In power spectra, we detect strong band-limited noise and varying low-frequency quasi-periodic oscillations that evolved from ~0.5 to ~5 Hz during the initial low/hard state of the source. We find that the second outburst closely resembled the spectral evolution of the first. The X-ray transient's overall outburst characteristics led us to classify XTE J1908+094 as a black hole candidate. Here we also derive precise X-ray position of the source using *Chandra* observations that were performed during the decay phase of the first outburst and following the second outburst.

Subject headings: accretion, accretion disks — black hole physics — stars: individual (XTE J1908+094)

On-line material: machine-readable table

1. INTRODUCTION

The X-ray transient source XTE J1908+094 was serendipitously discovered on 2002 February 19 during scheduled *Rossi X-Ray Timing Explorer* (*RXTE*) Proportional Counter Array (PCA) observations of a soft gamma repeater, SGR 1900+14 (Woods et al. 2002). Subsequent *RXTE* PCA scanning observations of the region allowed the localization of the new source to R.A. = $19^h08^m50^s$, decl. = $+09°22'30''$ with an accuracy of $2'$. This placed the new source about $24'$ away from SGR 1900+14. Based on Very Large Array observations on 2002 March 21 and 22, a transient source was suggested as the radio counterpart candidate to XTE J1908+094 (Rupen et al. 2002a). Observations in the optical band on April 8 and 9 revealed no new sources near the radio position (Garnavich et al. 2002); however, Chaty et al. (2002) identified a near-infrared counterpart to the new source and concluded that XTE J1908+094 is in a low-mass X-ray binary system with a main-sequence companion of spectral type later than K. Based on our preliminary analysis of the *RXTE* PCA observations, we concluded that XTE J1908+094 is a new stellar mass black hole candidate (Woods et al. 2002).

There are currently 18 dynamically confirmed and 20 candidate stellar mass black hole systems in our Galaxy (see McClintock & Remillard 2004 for a recent review). Most of them are characterized by occasional transient outbursts (X-ray novae; Chen et al. 1997) as a result of sudden increase in the mass accretion rate possibly triggered by instabilities in the accretion disk (Cannizzo 1993; Dubus et al. 2001). During outbursts, these systems generally undergo various changes in their spectral characteristics, usually in conjunction with changes in their timing behavior (see, e.g., Homan et al. 2001). The most common black hole (BH) spectral states are (1) the low/hard state, in which the spectrum is represented by a hard power law and usually accompanied by timing variability, and (2) the thermal-dominant (high/soft) state, in which a blackbody appears in the spectrum as the power-law component gets steeper and timing features get weaker or completely disappear (Tanaka & Lewin 1995). Other spectral states characterized by more complicated spectral and timing properties are also observed (e.g., Homan et al. 2001).

In this study, we present the results of our spectral and timing analysis of the *RXTE* pointed observations of XTE J1908+094 covering two outburst episodes. We also report observations with the *Chandra X-Ray Observatory* taken under Director's Discretionary Time (DDT). We describe our observations in § 2, and we present detailed data analyses in § 3. In § 4 we discuss and compare the different states of the source to other black hole candidates.

2. OBSERVATIONS

In Figure 1, we show the light curve of XTE J1908+094 in the 1.5–12 keV band observed with the All Sky Monitor (ASM) on board *RXTE*. Pointed observations with *RXTE*, indicated by vertical lines, were made throughout two outburst episodes until 2003 January 31, although pointings were more frequent during the first outburst. In this study, we used the data from 58 pointed *RXTE* observations (Observations No. 7–64 in Table 1) with a total exposure time of 110.4 ks. In addition, we have six observations of SGR 1900+14 from our monitoring program (No. 1–6 in Table 1), covering the same portion of the sky ~40 days prior to the first transient outburst of XTE J1908+094. We use these pointings to determine the background behavior from other sources in the field and

[1] Sabancı University, Orhanlı-Tuzla 34956, İstanbul, Turkey; ersing@sabanciuniv.edu.
[2] Universities Space Research Association.
[3] National Space Science and Technology Center, 320 Sparkman Drive, Huntsville, AL 35805.
[4] NASA Marshall Space Flight Center, SD-50, Huntsville, AL 35812.
[5] National Research Council Fellow.
[6] NRAO, Socorro, NM 87801.
[7] NASA Goddard Space Flight Center, Greenbelt, MD 20771.
[8] Astronomical Institute "Anton Pannekoek" and CHEAF, University of Amsterdam, 403 Kruislaan, NL-1098 SJ Amsterdam, Netherlands.

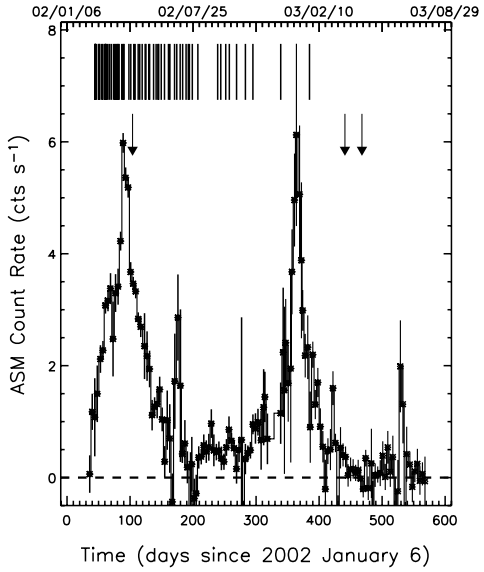

FIG. 1.—Light curve of XTE J1908+094 as seen in 1.5–12 keV with the *RXTE* ASM. The vertical lines indicate the times of pointed *RXTE* observations of the source. The arrows denote the times of *Chandra* pointings. Observation times are relative to 2002 January 6 (MJD 52,280). The calendar dates indicated above are in YY/MM/DD format.

the Galactic ridge contribution as described in § 3.3. For convenience, we reference all times to 2002 January 6 (MJD 52,280) in this paper.

In addition to the ASM, there are two more instruments on board *RXTE*: the PCA, an array of five nearly identical Proportional Counter Units (PCUs), which are sensitive to photon energies between 2 and 60 keV, and the High-Energy X-Ray Timing Experiment (HEXTE), which is sensitive to photon energies between 15 and 250 keV. Here, we present the results of our PCA data analysis only. The HEXTE spectral data analysis resulted in large statistical uncertainties after the background subtraction, even during the phase when the hard spectral component dominates the source spectrum, and it is not presented.

A short (1.1 ks) *Chandra* Advanced CCD Imaging Spectrometer (ACIS) observation was performed on 2002 April 15. It took place during the relatively bright phase of the outburst (day 99 in Fig. 1), resulting in heavy pileup. Nevertheless, we could still use the data to determine an accurate X-ray position of XTE J1908+094. There are additionally two publicly available *Chandra* ACIS pointings performed on 2003 March 23 and April 19 for ~4.7 ks each. We used these observations to confirm our best location solution determined from the earlier short pointing.

TABLE 1
RXTE OBSERVATIONS OF XTE J1908+094

Observation Number	Time[a]	Exposure (ks)	Count Rate[b] (counts s^{-1} PCU^{-1})	Hardness Ratio[c]	Observation Number	Time[a]	Exposure (ks)	Count Rate[b] (counts s^{-1} PCU^{-1})	Hardness Ratio[c]
1	0.1	9.9	<0.09	...	33	115.4	1.2	11.6	0.035(3)
2	1.2	10.0	<0.09	...	34	119.3	0.6	13.0	0.048(3)
3	1.6	9.7	<0.04	...	35	123.9	1.3	8.1	0.043(6)
4	2.1	10.2	<0.06	...	36	125.2	0.8	7.6	0.034(8)
5	5.2	9.8	<0.04	...	37	129.9	0.9	8.7	0.058(5)
6	11.1	10.0	<0.02	...	38	131.1	1.6	6.4	0.037(3)
7	44.9	9.4	12.1	0.224(3)	39	137.4	1.1	3.8	0.042(8)
8	46.4	3.0	13.4	0.199(3)	40	141.3	1.1	6.2	0.080(6)
9	49.7	2.9	15.7	0.223(2)	41	144.2	1.6	7.0	0.090(4)
10	50.7	2.9	16.5	0.226(2)	42	145.5	1.7	6.8	0.099(4)
11	51.9	2.9	18.1	0.201(3)	43	149.5	0.9	7.4	0.132(4)
12	54.9	3.3	21.4	0.207(1)	44	154.6	1.1	5.4	0.182(8)
13	56.9	3.3	24.3	0.207(1)	45	160.9	0.7	5.0	0.169(8)
14	60.7	8.9	29.6	0.215(1)	46	163.2	0.6	4.8	0.177(9)
15	62.2	2.1	31.5	0.212(1)	47	170.5	1.3	3.5	0.165(9)
16	64.4	1.5	32.3	0.209(1)	48	174.2	1.1	3.7	0.171(8)
17	67.2	1.2	33.3	0.215(2)	49	179.4	1.0	3.4	0.122(8)
18	70.1	3.1	33.8	0.208(1)	50	183.3	0.9	3.1	0.114(7)
19	73.6	2.4	35.3	0.194(1)	51	188.9	1.6	3.2	0.147(8)
20	75.8	0.9	36.6	0.190(2)	52	192.4	0.7	2.9	0.090(18)
21	77.8	1.4	35.3	0.193(1)	53	194.2	1.2	2.6	0.107(15)
22	79.9	3.4	35.8	0.200(1)	54	198.8	1.8	2.6	0.181(9)
23	80.9	3.2	35.1	0.193(1)	55	207.6	1.1	2.2	0.133(10)
24	82.7	1.9	37.8	0.175(1)	56	238.9	0.9	2.5	0.158(20)
25	86.8	1.9	39.0	0.139(1)	57	244.0	1.2	2.4	0.148(11)
26	88.9	2.5	38.1	0.084(1)	58	251.8	0.8	2.6	0.159(19)
27	90.5	1.6	41.6	0.048(1)	59	257.5	1.9	2.6	0.151(13)
28	98.2	1.4	26.2	0.029(1)	60	269.0	1.9	2.2	0.177(14)
29	101.2	1.5	20.7	0.018(1)	61	283.1	1.6	2.7	0.163(9)
30	105.9	1.9	15.3	0.013(1)	62	295.0	1.2	2.8	0.172(9)
31	107.9	0.9	16.0	0.005(2)	63	339.1	1.4	11.4	0.203(3)
32	112.9	3.1	13.7	0.019(1)	64	384.7	1.5	10.1	0.032(2)

[a] Observation times referenced to 2002 January 6.0 (MJD 52,280.0).
[b] Background-subtracted, orbit-averaged rates in the 2–20 keV band.
[c] Hardness ratios defined as the ratio of the background-subtracted, orbit-averaged rates in the 10–20 keV band to those in the 2–10 keV band.

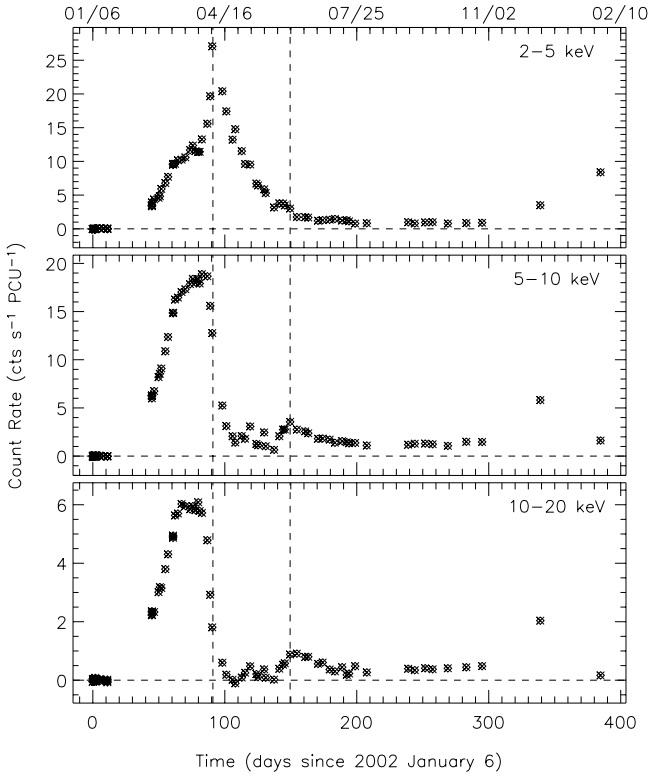

FIG. 2.—Light curves of XTE J1908+094 as seen in the 2–5, 5–10, and 10–20 keV ranges. Each point represents the averaged and background-subtracted count rates of each *RXTE* PCA orbit in a given energy interval. The dashed vertical lines indicate the times of spectral state transitions, from hard to soft (*left*), and soft to hard (*right*). The calendar dates indicated above are in MM/DD format.

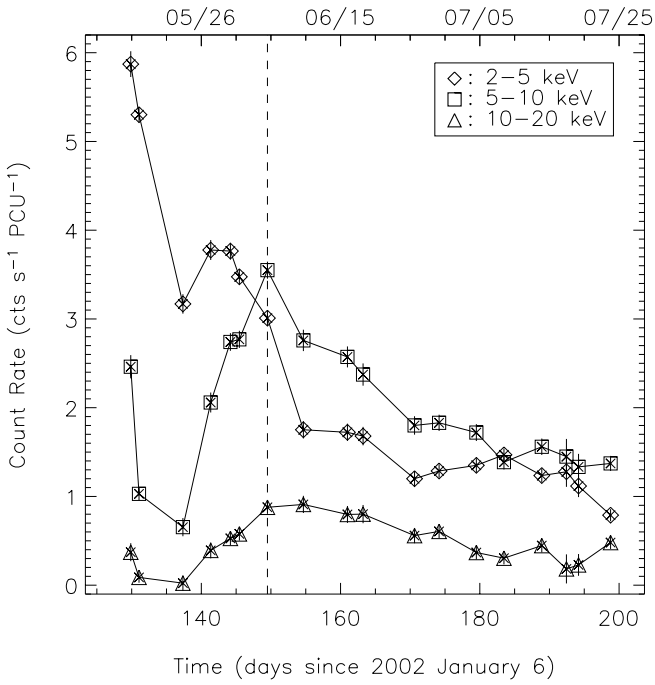

FIG. 3.—Zoom-up of the XTE J1908+094 light curves around the time of the secondary peak in three energy bands. The calendar dates indicated above are in MM/DD format.

3. DATA ANALYSIS AND RESULTS

3.1. *Source Location from the Chandra ACIS Data*

Our 2002 *Chandra* observation was taken in the ACIS full-frame timed exposure mode while the two subsequent observations were collected in the 1/8 subarray mode. Initial standard processing of the data was performed by the *Chandra* X-Ray Center (CXC). We modified the standard processed data by using *acis_process_events* (CIAO, ver. 2.3) to remove pixel randomization and to retrieve X-ray events flagged bad while attempting to remove cosmic-ray events. The data were filtered to exclude events with ASCA grades 1, 5, and 7, hot pixels, bad columns, and events on CCD node boundaries.

To determine the location of XTE J1908+094, we followed the method of Hulleman et al. (2001) and fitted the piled-up image with an appropriate function. We also determined the position from the two observations in 2003 and found that they are consistent. Since these data were not significantly piled-up, we fitted a two-dimensional Gaussian to the source location and determined the source centroid. We averaged all these locations and derived a (J2000.0) position of $\alpha = 19^{\rm h}08^{\rm m}53\overset{\rm s}{.}07$, $\delta = +09^\circ 23' 04\overset{''}{.}9$ for XTE J1908+094 (90% error radius of $0\overset{''}{.}6$).[9]

3.2. *Light Curves, Hardness Ratios, and Color-Intensity Diagram*

In Figure 2, we show the long-term PCA light curves of XTE J1908+094 in the 2–5, 5–10, and 10–20 keV energy bands. During the first ~16 days of the outburst (from day 44 to 60 in Fig. 2), the rates in all three bands increased by a factor of ~3. In the following ~27 days, the rise was gradual in the 2–5 and 5–10 keV bands, while the 10–20 keV rate remained constant.

Starting at day ~87, the rate in the 2–5 keV range increased rapidly (by a factor of 2 over the next 3 days) and then decayed exponentially (*e*-folding time of 26.8 ± 1.2 days). During the time of the low-energy peak (Fig. 2, *left dashed vertical lines*), the rates in both higher energy bands sharply declined.

About 55 days after the low-energy peak, we see a secondary peak in all three energy bands, possibly a secondary maximum often seen in X-ray novae (Chen et al. 1997). A closer look at the secondary peak (shown in Fig. 3) indicates that it evolves from soft to hard, with the 2–5 keV band peaking about 3 days earlier than the 5–10 keV energy band. It is noteworthy that soon after this secondary peak, the source transitioned into a harder spectral state (Fig. 2, *right dashed vertical line*; see also Fig. 3).

Between days 170 and 295, the source intensity remained very low (the flux varied between 1.6 and 3.6×10^{-10} ergs s^{-1} cm^{-2}) but significantly above the background value. (see Figs. 1 and 2). The last two PCA observations of XTE J1908+094 were during the second outburst episode, which took place between days ~330 and 410 (Fig. 1). The peak of the outburst as seen with the ASM is between these two observations.

Changes in the source spectral properties are also reflected in the hardness ratios, as illustrated in Figure 4. Here, the hardness ratios are defined as the ratio of the averaged (over each observation) count rates in the higher energy band to those in the lower energy band. Note that the evolution of the soft color (Fig. 4, *top panel*) and the hard color (Fig. 4, *middle panel*) are quite similar. The rise in hardness after the dip coincides with the secondary peak shown earlier (Fig. 4, *right dashed vertical line*).

We present a color-color diagram in Figure 5. The different colors of the symbols correspond to the spectral states of the

[9] Additional information from the *Chandra* X-Ray Center is available at http://asc.harvard.edu/cal/ASPECT/celmon.

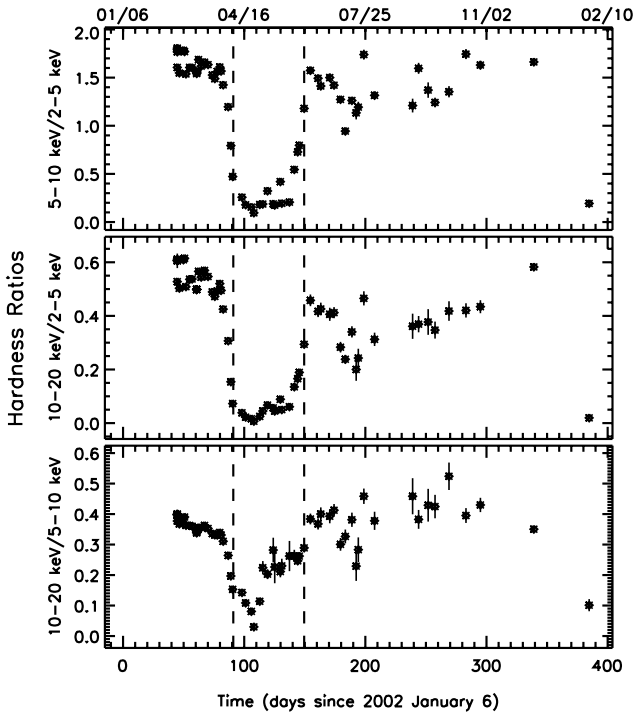

FIG. 4.—Evolution of the hardness ratios in XTE J1908+094 defined as the ordinate names of each panel. The calendar dates indicated above are in MM/DD format.

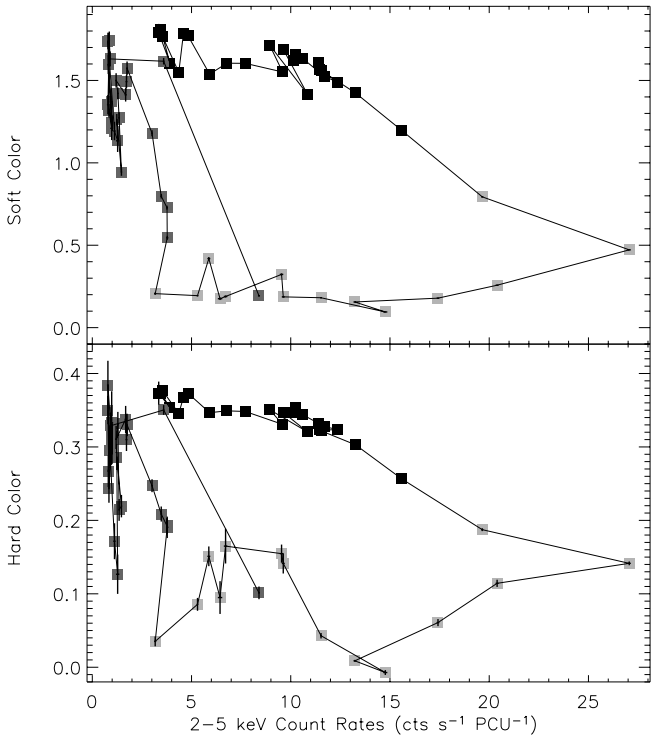

FIG. 6.—Color-intensity diagram for the soft (*top*) and the hard colors (*bottom*).

source; black represents the early hard state (days 44–90), and these points are therefore concentrated at the top right corner of the diagram. Light gray represents the soft state (days 90–140), and dark gray represents points from the subsequent low state (days 140–afterward).

In Figure 6, we show the color-intensity diagram for both the soft and hard colors. Colors are identical to those in Figure 5. After the onset of the first outburst, both colors remained at high levels, then decreased quickly as the source underwent the first state transition and looped in the clockwise direction. Note that the color of the first of the last two observations appears to be at the level of the initial hard state, and the color of the last observation is among those in the soft state. Therefore, the second outburst, like the first, transitioned from a hard to a soft spectral state.

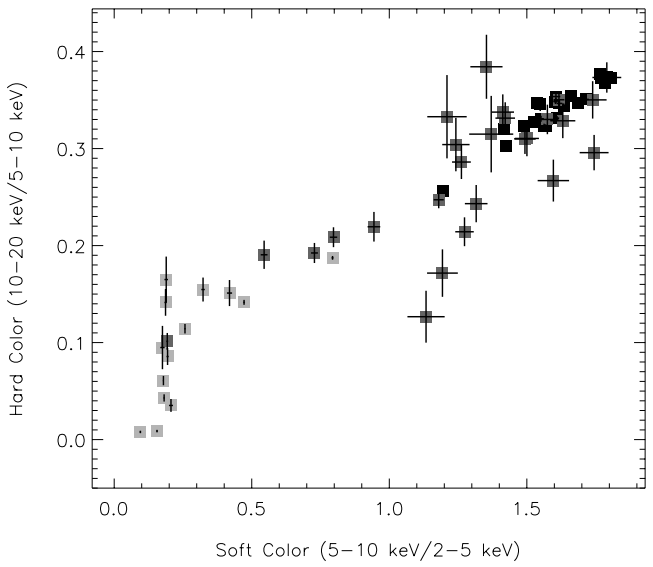

FIG. 5.—Color-color diagram of XTE J1908+094. The hard color is the ratio of (background-subtracted) rates in the 10–20 keV to the 5–10 keV band for each observing window, and the soft color is the ratio of those in the 5–10 keV to the 2–5 keV band.

3.3. *Spectral Analysis*

For each *RXTE* observing orbit, we extracted the PCA spectrum using Standard2 data (129 channels accumulated every 16 s) collected from the top layer of all operating PCUs (to achieve the highest signal-to-noise ratio), excluding PCU0 (because of its higher background level caused by the loss of its propane layer). In selecting data we required the Earth elevation angle to be greater than 10° and the time to the nearest South Atlantic Anomaly passage to be greater than 30 minutes. A background spectrum was generated using the faint source background models provided by the PCA instrument team and *pcabackest*, which is an FTOOLS utility. Spectral modeling was performed using XSPEC version 11.2.0.

Because the PCA is not an imaging instrument and has a relatively large field of view (≈1° FWHM), the background-subtracted PCA spectra of XTE J1908+094 still have some contamination from other X-ray sources in the field and from the Galactic ridge. To determine the spectral shape and the intensity level of this contamination, we generated background-subtracted spectra from the PCA observations performed ∼40 days before the outburst (Obs. No. 1–6 in Table 1) using the same methodology described earlier. We found that all these spectra were well fitted by a power law ($\Gamma = 1.8$) plus a Gaussian line ($E_{\rm cent} = 6.68$ keV and $E_{\rm width} = 0.45$ keV) both attenuated by the interstellar absorption (fixed at $N_{\rm H} = 1.8 \times 10^{22}$ cm^{-2}, as given by Valinia & Marshall 1998). The model normalizations of all six spectral fits are consistent within errors; therefore, we calculated their weighted mean (by statistical errors). We then included this absorbed power law plus

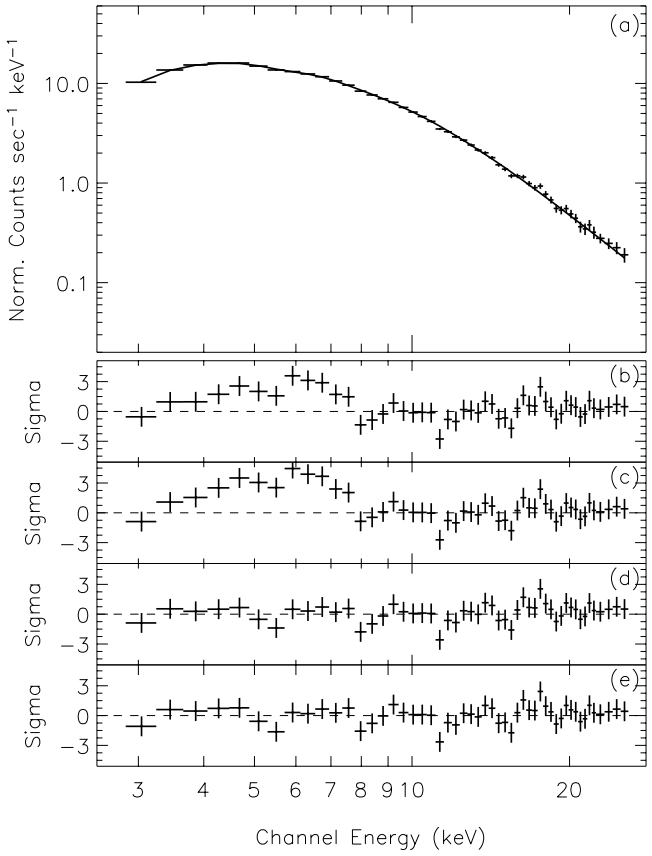

FIG. 7.—Representative spectral fit of a PCA observation during the early hard state of XTE J1908+094 (on day 62). (*a*) Count spectrum and the best-fit multicolor disk blackbody (MCD) + broad line + power law model all attenuated by the interstellar absorption (*solid line*). (*b*) Residuals of the best-fit single power-law model ($\chi^2_\nu = 1.87$). (*c*) Residuals of the best-fit MCD + power law model ($\chi^2_\nu = 2.66$). (*d*) Residuals of the best-fit broad line + power law model ($\chi^2_\nu = 0.88$). (*e*) Residuals of the best-fit MCD + broad line + power law model ($\chi^2_\nu = 0.87$).

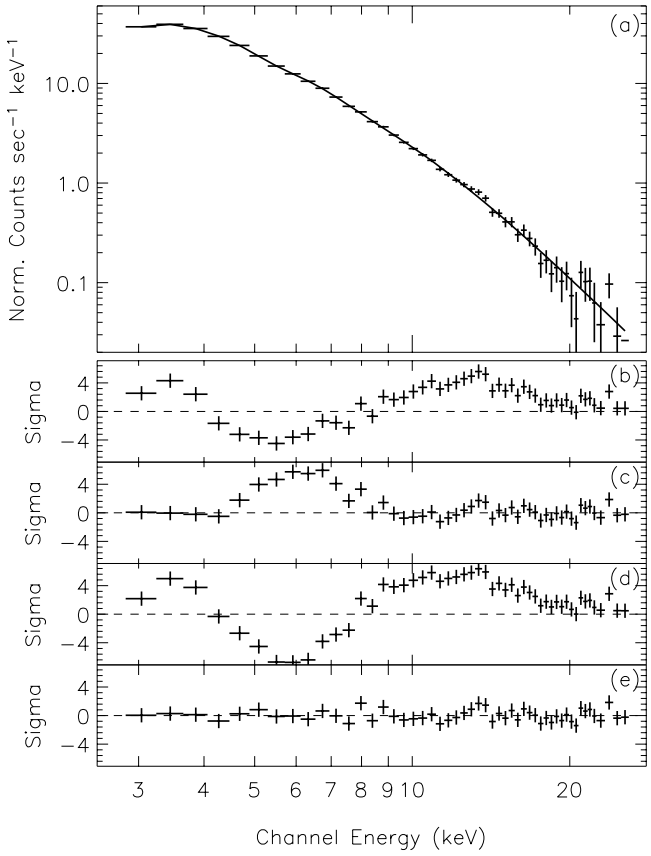

FIG. 8.—Representative spectral fit of a PCA observation during the intermediate state of XTE J1908+094 (on day 90). (*a*) Count spectrum and the best-fit multicolor disk blackbody (MCD) + broad line + power law model all attenuated by the interstellar absorption (*solid line*). (*b*) Residuals of the best-fit single power-law model ($\chi^2_\nu = 8.26$). (*c*) Residuals of the best-fit MCD + power law model ($\chi^2_\nu = 4.17$). (*d*) Residuals of the best-fit broad line + power law model ($\chi^2_\nu = 14.50$). (*e*) Residuals of the best-fit MCD + broad line + power law model ($\chi^2_\nu = 0.70$).

Gaussian line model (all parameters are fixed at determined values) as a fixed term in the subsequent spectral fitting of the XTE J1908+094.

The energy spectra of the black hole X-ray binaries are generally successfully fitted by a two-component model containing a multicolor disk blackbody (Mitsuda et al. 1984) plus a power law (Tanaka & Lewin 1995). The former (or soft) component is expected to originate mainly from the inner portions of the accretion disk ($T_{\rm disk} \propto R^{-3/4}$), while the latter (hard) component is believed to be due to Compton upscattering of low-energy seed photons from the disk by the energetic electrons (possibly) in the hot corona around the inner disk.

Our initial fits to each XTE J1908+094 spectrum (over the energy range of 2.5–25 keV) with absorbed ($N_{\rm H}$ fixed at 2.5×10^{22} cm^{-2} as reported by in't Zand et al. 2002) disk blackbody plus power law model during the early hard state of the outburst (from days 44 to 90) revealed a significant excess in the resulting residuals between 4.5 and 7 keV. Inclusion of a Gaussian line component to the model resulted in a broad-line feature (see the two representative spectra in Figs. 7 and 8 for the necessity of adding this component) and significant improvement in the goodness of fit to the acceptable level. Also during this state, the disk blackbody component was not statistically required; nonetheless, we kept this component to determine the upper limits of the disk blackbody flux. Table 2 lists the resulting values for the spectral parameters. In all spectral fits, we obtained statistically acceptable χ^2_ν values ranging between 0.51 and 1.19.

We show the variations of the spectral model parameters in Figure 9. During the low/hard state, the power-law index remained fairly constant ($\Gamma \sim 1.5$). The centroid of the broad-line feature appears to vary between 5.18 and 6.88 keV, with a statistically weighted average of 5.73 ± 0.09 keV. The width of the line ranges between 0.96 and 1.27 keV, with a weighted average value of 1.11 ± 0.31 keV. The corresponding line equivalent widths range from 153 to 734 eV, with the majority being between 170 and 360 eV.

As the source transited into the soft state (Fig. 9, *first dashed line*), the disk blackbody component appeared and became prominent, while the broad-line feature disappeared. The blackbody temperature clearly evolves during the soft state. The model normalization, $N_{\rm disk}$, of the disk blackbody component is parameterized in terms of the inner-disk radius, the distance to the source, and the inclination angle, as $N_{\rm disk} = (R^2_{\rm in,km}/d^2_{10\ \rm kpc}) \cos\theta$. If the last two are assumed to not vary over the course of the soft spectral state, there is some evidence for an early increase of the inner-disk radius that remains relatively constant around ~40 until day 130 and then decreases to its initial value. Meanwhile, the power-law trend became steeper with an average value of $\Gamma \sim 2.5$.

On day ~149, soon after the secondary peak (Fig. 9, *second dashed line*), the spectral transition into the low/hard state

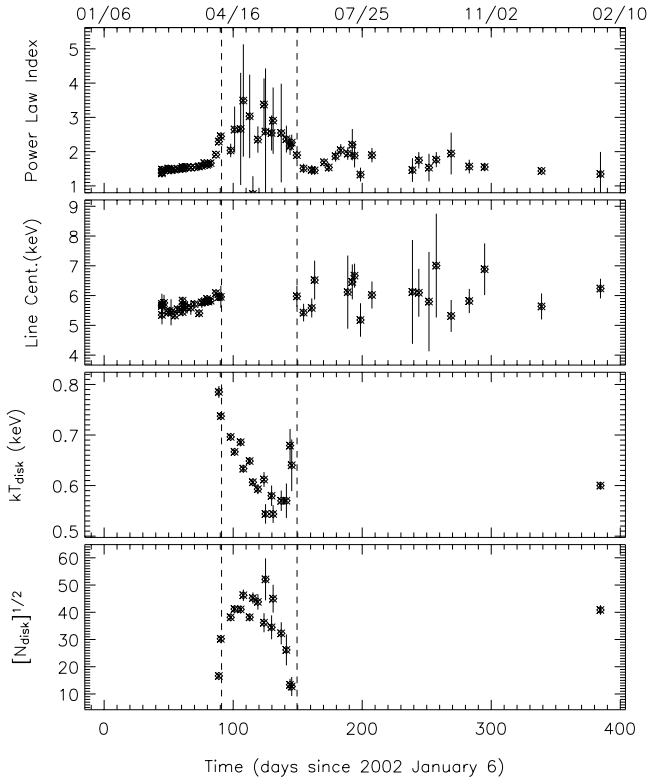

FIG. 9.—Time history of the spectral model parameters.

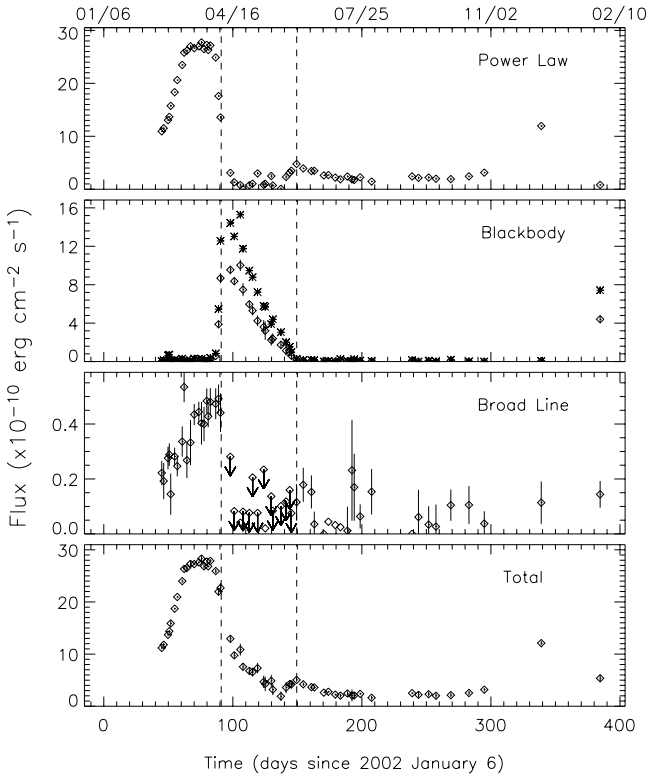

FIG. 10.—Time history of the absorbed fluxes of each model component integrated over the 2.5–25 keV range. The blackbody flux values integrated over the 1–25 keV are shown with asterisks in the second panel from the top. The upper flux limits of the broad-line feature indicate the 2 σ level.

took place. Similar to the earlier hard state, the source spectrum is dominated by the power-law component and the broad-line feature again becomes observable, although with relatively lower line flux and therefore with larger uncertainties in the line model parameters (see also Fig. 10).

The last two *RXTE* observations studied here (on days 339 and 384) captured a glimpse of the second outburst; the first of these pointings was during the rise of the X-ray intensity, while the second was during its decline (see Fig. 1). Detailed spectral analysis of these two observations show that the spectrum of the first one was hard, resembling the low/hard state; in contrast, the spectrum of the second was strongly dominated by the soft component, indicating the reappearance of disk emission.

Figure 10 illustrates the time history of the fluxes of each model component. Similar to the 10–20 keV light curve of the source (Fig. 2, *bottom panel*), the power-law flux increased over the first 16 days into the outburst, then remained constant, forming the "knee" at around day 60. There is an apparent correlation between the line and power-law fluxes (especially during the first rising portion and around the secondary peak), which suggests that these two may be related.

In the 2.5–25 keV energy range, in which the spectral fitting was performed, we have been detecting only the higher energy tail of the blackbody spectrum ($kT \sim 0.6$–0.7 keV) whose significant portion lies between 1 and 2.5 keV. To account for this, we have additionally integrated the blackbody flux values over 1–25 keV (Fig. 10, *asterisks in second panel from the top*). We find that the absorbed 1–25 keV disk flux is ~50% larger than the flux in the 2.5–25 keV range.

3.4. *Timing Analysis*

We computed power spectra for each pointed observation using the PCA event-mode data (E_125us_64M_1s). In the few cases in which more than one PCU combination occurred during an observation, we made separate power spectra for each combination. More specifically, we generated light curves from the event mode data using 31.25 ms binning and divided them into 512 s segments, which were then Fourier transformed. The Fourier powers were then averaged over the segments.

To examine the overall evolution of the source noise during the first outburst, we generated power spectra in three energy bands: 2–5, 5–10, and 10–20 keV. Figure 11 shows the fractional rms amplitude in the 0.002–5 Hz frequency range for each energy band during the first outburst. The rms amplitudes were normalized to the source count rates obtained by subtracting from the observed count rate the faint source model rate and the predicted rate from the Galactic ridge emission. There is no significant difference between energy bands. The fractional variability drops slowly until day 87, after which it falls rapidly in coincidence with the fall of the 10–20 keV flux and the rapid rise in the 2–5 keV flux. After the peak of the 2–5 keV flux on day 90, the source noise power is no longer detected.

Figure 12 shows a representative power spectrum (from the observation on day 55) for the 2–20 keV energy band. The top panel shows the Leahy normalized power with the Poisson noise level of 2 subtracted. For better display this has been logarithmically rebinned in frequency. At low frequencies the power spectrum is nearly flat, while at high frequencies it drops off as a power law with index near -1. In the bottom panel we plot the power minus Poisson noise level multiplied by the frequency, which is proportional to the source power per decade of frequency. Evident in this plot is a quasi-periodic oscillation (QPO) near 0.5 Hz.

TABLE 2

SPECTRAL FIT PARAMETERS

	MULTICOLOR DISK BLACKBODY			BROAD LINE			POWER LAW		
OBSERVATION NUMBER	kT_{disk}[a] (keV)	N_{disk}	F_{disk}[b] (10^{-10} cgs)	$E_{cent.}$[a] (keV)	σ[a] (keV)	F_{line}[b] (10^{-11} cgs)	Γ	F_{PL}[b] (10^{-9} cgs)	F_{Total}[b] (10^{-9} cgs)
7.....	0.60	<11.5	<0.03	5.72 ± 0.17	1.07 ± 0.55	2.21(44)	1.40 ± 0.03	1.09(1)	1.12(2)
8.....	0.60	<39.5	<0.09	5.75 ± 0.27	1.03 ± 0.92	1.92(66)	1.45 ± 0.04	1.15(2)	1.18(4)
9.....	0.60	<149.7	<0.35	5.44 ± 0.14	0.96 ± 0.44	2.76(41)	1.50 ± 0.03	1.30(1)	1.37(2)
10.....	0.60	<170.0	<0.40	5.49 ± 0.13	0.96 ± 0.43	2.88(41)	1.49 ± 0.02	1.36(1)	1.44(2)
11.....	0.60	<0.01	<0.01	5.44 ± 0.43	1.10 ± 1.35	1.44(75)	1.45 ± 0.03	1.57(2)	1.59(5)
12.....	0.60	<47.1	<0.11	5.33 ± 0.11	1.16 ± 0.34	2.81(32)	1.47 ± 0.01	1.83(1)	1.87(2)
13.....	0.60	<31.6	<0.07	5.54 ± 0.12	1.25 ± 0.43	2.46(37)	1.50 ± 0.01	2.06(1)	2.09(2)
14.....	0.60	<76.9	<0.02	5.60 ± 0.15	1.14 ± 0.50	3.36(55)	1.55 ± 0.02	2.34(2)	2.39(3)
15.....	0.60	<0.01	<0.01	5.68 ± 0.11	1.31 ± 0.37	5.34(55)	1.52 ± 0.01	2.57(2)	2.63(4)
16.....	0.60	<37.2	<0.08	5.61 ± 0.21	1.14 ± 0.69	2.68(65)	1.55 ± 0.02	2.61(2)	2.65(3)
17.....	0.60	<0.01	<0.01	5.59 ± 0.23	1.10 ± 0.76	3.32(82)	1.53 ± 0.02	2.69(3)	2.73(6)
18.....	0.60	<78.3	<0.18	5.71 ± 0.08	1.11 ± 0.29	4.34(38)	1.54 ± 0.01	2.66(1)	2.73(2)
19.....	0.60	<68.1	<0.16	5.41 ± 0.09	1.15 ± 0.28	4.44(37)	1.57 ± 0.01	2.69(1)	2.76(2)
20.....	0.60	<69.3	<0.17	5.77 ± 0.18	1.12 ± 0.62	4.02(78)	1.58 ± 0.02	2.77(3)	2.83(5)
21.....	0.60	<0.01	<0.01	5.78 ± 0.14	1.12 ± 0.49	3.99(62)	1.66 ± 0.01	2.64(2)	2.68(4)
22.....	0.60	<0.01	<0.01	5.89 ± 0.09	1.27 ± 0.32	4.84(46)	1.61 ± 0.01	2.72(1)	2.78(2)
23.....	0.60	<29.6	<0.07	5.80 ± 0.08	1.11 ± 0.30	4.28(40)	1.64 ± 0.01	2.63(1)	2.68(2)
24.....	0.60	<97.8	<0.23	5.83 ± 0.10	1.10 ± 0.35	4.80(50)	1.66 ± 0.01	2.71(2)	2.79(3)
25.....	0.75	<55.4	<0.58	6.08 ± 0.11	1.10 ± 0.39	4.73(56)	1.91 ± 0.02	2.48(2)	2.59(4)
26.....	0.79 ± 0.01	276 ± 27	3.88(37)	5.95 ± 0.07	1.10 ± 0.33	4.91(52)	2.29 ± 0.03	1.76(2)	2.19(7)
27.....	0.74 ± 0.01	914 ± 55	8.67(52)	5.96 ± 0.37	1.20 ± 0.48	4.40(70)	2.44 ± 0.06	1.35(2)	2.27(9)
28.....	0.69 ± 0.01	1455 ± 69	9.55(45)	6.0	1.15 ± 0.55	<2.80	2.03 ± 0.19	0.31(3)	1.29(8)
29.....	0.67 ± 0.01	1696 ± 84	8.37(42)	6.0	0.67 ± 1.55	<0.83	2.64 ± 0.67	0.13(2)	0.98(7)
30.....	0.69 ± 0.01	1686 ± 99	10.0(59)	6.0	1.10	<0.41	2.66 ± 1.64	0.08(2)	1.09(11)
31.....	0.63 ± 0.01	2139 ± 193	7.48(68)	6.0	0.62 ± 1.14	<0.81	3.49 ± 1.64	0.01(3)	0.76(7)
32.....	0.65 ± 0.01	1456 ± 76	5.96(31)	6.0	1.07 ± 2.10	<0.77	3.03 ± 1.22	0.08(0)	0.68(7)
33.....	0.61 ± 0.01	2045 ± 188	5.30(49)	6.0	1.00 ± 0.62	<2.05	0.76 ± 0.51	0.10(2)	0.66(7)
34.....	0.59 ± 0.01	1920 ± 251	4.24(55)	6.0	0.67 ± 2.89	<0.76	2.35 ± 0.38	0.29(3)	0.73(10)
35.....	0.61 ± 0.01	1308 ± 253	3.60(70)	6.0	1.14 ± 0.71	<2.34	3.37 ± 0.76	0.08(4)	0.47(12)
36.....	0.54 ± 0.01	2713 ± 803	3.21(95)	6.0	1.10	<0.20	2.58 ± 1.84	0.10(3)	0.43(14)
37.....	0.58 ± 0.02	1189 ± 303	2.24(57)	6.0	1.15 ± 1.97	<1.36	2.54 ± 0.51	0.25(3)	0.49(11)
38.....	0.54 ± 0.02	2024 ± 461	2.39(54)	6.0	1.36 ± 2.57	<0.84	2.90 ± 0.97	0.07(3)	0.32(10)
39.....	0.57 ± 0.02	1042 ± 263	1.73(44)	6.0	0.88 ± 2.16	<1.01	2.54 ± 1.44	0.08(3)	0.19(9)
40.....	0.57 ± 0.04	686 ± 297	1.14(50)	6.0	1.43 ± 2.39	<1.18	2.36 ± 0.39	0.23(3)	0.36(11)
41.....	0.68 ± 0.03	178 ± 59	0.99(33)	6.0	1.10 ± 1.14	<1.59	2.16 ± 0.26	0.31(2)	0.43(7)
42.....	0.64 ± 0.05	163 ± 89	0.61(33)	6.0	1.32 ± 2.78	<0.76	2.26 ± 0.23	0.35(2)	0.42(8)
43.....	0.60	<69.9	<0.17	5.97 ± 0.35	1.09 ± 1.39	1.15(66)	1.89 ± 0.08	0.48(2)	0.50(3)
44.....	0.60	<37.8	<0.10	5.43 ± 0.29	1.10 ± 0.93	1.78(62)	1.51 ± 0.14	0.39(2)	0.42(3)
45.....	0.60	<35.7	<0.09	5.59 ± 0.32	1.08 ± 1.03	1.52(60)	1.46 ± 0.15	0.34(2)	0.37(3)
46.....	0.60	<40.3	<0.09	6.52 ± 0.65	1.10	0.35(46)	1.45 ± 0.13	0.35(1)	0.36(3)
47.....	0.60	<0.01	<0.001	6.0	1.10	<0.01	1.68 ± 0.06	0.26(1)	0.26(1)
48.....	0.60	<19.0	<0.04	6.0	1.10	<0.44	1.53 ± 0.12	0.27(1)	0.28(2)
49.....	0.60	<0.01	<0.001	6.0	1.10	<0.32	1.86 ± 0.16	0.22(1)	0.22(2)
50.....	0.60	<61 1	<0.14	6.0	1.10	<0.25	2.04 ± 0.17	0.19(2)	0.20(4)
51.....	0.60	<17.3	<0.04	6.12 ± 1.22	1.06 ± 1.58	2.12(87)	1.94 ± 0.18	0.24(2)	0.25(4)
52.....	0.60	<0.01	<0.01	6.46 ± 0.58	1.41 ± 2.08	2.31(1.84)	2.20 ± 0.46	0.19(5)	0.21(12)
53.....	0.60	<61.1	<0.15	6.67 ± 0.40	1.09 ± 1.83	1.69(1.22)	1.88 ± 0.35	0.18(3)	0.20(7)
54.....	0.60	<23.5	<0.06	5.18 ± 0.56	0.82 ± 1.59	0.64(44)	1.33 ± 0.20	0.22(1)	0.24(2)
55.....	0.60	<9.84	<0.02	6.02 ± 0.45	1.82 ± 1.66	1.53(83)	1.89 ± 0.21	0.15(1)	0.16(3)
56.....	0.60	<37.7	<0.09	6.12 ± 1.74	1.10	<0.01	1.46 ± 0.35	0.24(2)	0.25(2)
57.....	0.60	<0.01	<0.01	6.09 ± 0.80	1.24 ± 3.74	0.61(99)	1.74 ± 0.23	0.21(2)	0.22(5)
58.....	0.60	<25.2	<0.06	5.79 ± 1.66	1.10	0.34(67)	1.53 ± 0.40	0.22(2)	0.23(4)
59.....	0.60	<0.01	<0.01	7.01 ± 1.74	1.10	0.27(80)	1.76 ± 0.22	0.19(2)	0.20(5)
60.....	0.60	<45.7	<0.11	5.32 ± 0.53	1.1 ± 1.41	1.04(57)	1.94 ± 0.61	0.19(2)	0.21(4)
61.....	0.60	<3.46	<0.08	5.82 ± 0.40	1.08 ± 1.62	1.05(69)	1.56 ± 0.20	0.24(2)	0.25(4)
62.....	0.60	<0.01	<0.01	6.88 ± 0.86	1.10	0.38(45)	1.55 ± 0.12	0.31(1)	0.32(3)
63.....	0.60	<15.0	<0.04	5.63 ± 0.43	1.28 ± 1.72	1.13(77)	1.43 ± 0.04	1.19(2)	1.20(4)
64.....	0.60 ± 0.01	1669 ± 144	4.40(38)	6.23 ± 0.33	1.08 ± 0.87	1.43(48)	1.34 ± 0.64	0.08(2)	0.54(7)

NOTE.—Table 2 is also available in machine-readable form in the electronic edition of the *Astrophysical Journal*.

[a] Values without errors were kept frozen in the fitting procedure.

[b] Absorbed flux in the 2.5–25 keV band. Values in the parentheses are the 2 σ level errors in the last number of digits of given flux values.

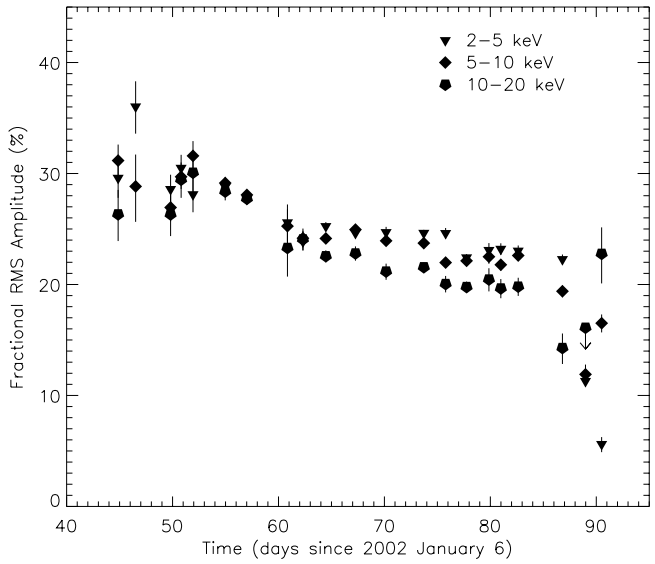

FIG. 11.—Fractional rms amplitudes determined for three energy ranges in frequencies between 0.002 and 5 Hz. The abrupt decline of the rms amplitudes in all three energy ranges coincides with the spectral transition from the low/hard state to the high/soft state.

We fitted the power spectra in the 2–20 keV band with a model with three components representing the Poisson level, the continuum, and the QPO,

$$P = A + B\left[\left(\frac{f}{f_0}\right)^{\alpha} + \left(\frac{f}{f_0}\right)^{\beta}\right]^{-1} + C\left[1 + 4\frac{\left(f - f_{\rm QPO}\right)^2}{\left(W_{\rm QPO}\right)^2}\right]^{-1}, \quad (1)$$

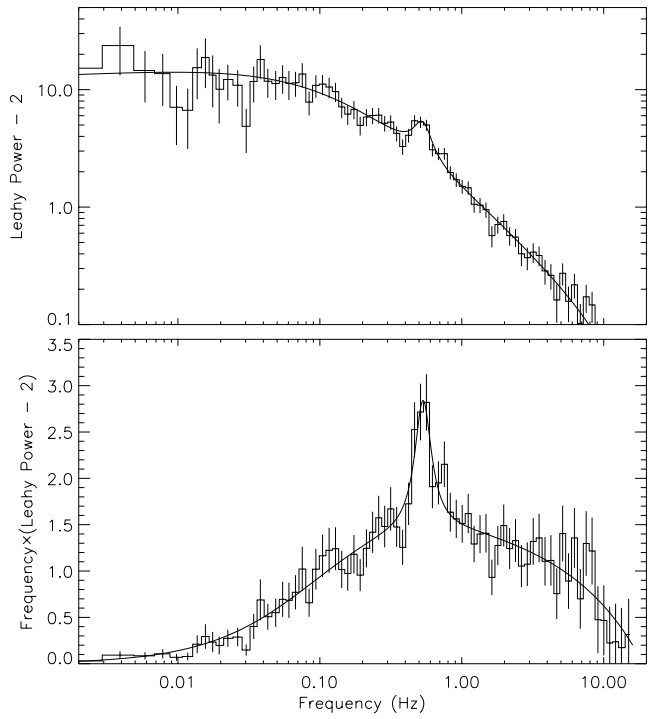

FIG. 12.—*Top*: Representative power spectrum of *RXTE* observations on day 54.9 (2002 March 1.9). *Bottom*: Same as top multiplied by the frequency. Notice the QPO peak at ~0.5 Hz.

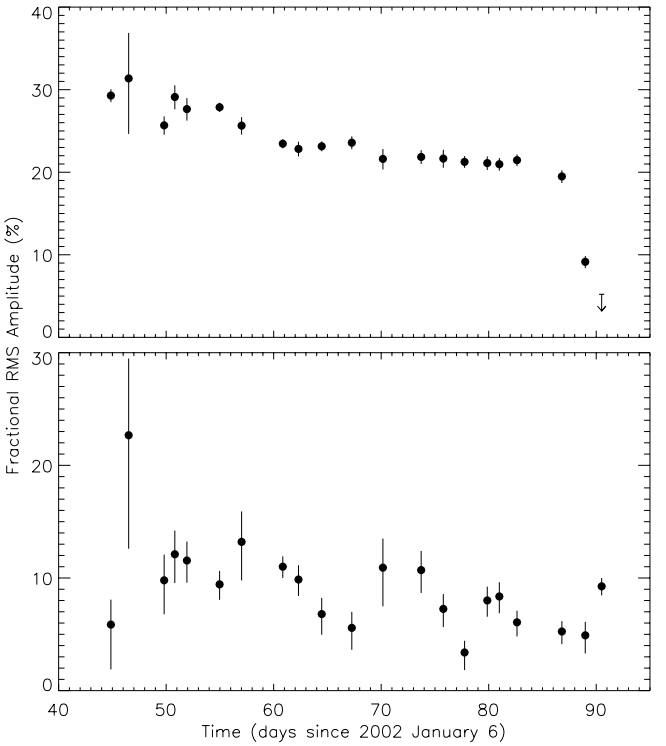

FIG. 13.—Time variation of the fractional rms amplitude of the continuum (*top*) and QPO components (*bottom*) in the 2–20 keV band. The indicated upper limit is at the 2 σ level.

where A, B, and C are the amplitudes of the Poisson level, continuum, and QPO components, f_0 is the break point in the continuum power-law index, α and β are the continuum index before and after the break, respectively, $f_{\rm QPO}$ is the QPO center, and $W_{\rm QPO}$ is the QPO FWHM. In general, this model reasonably characterized the power spectra.

Figure 13 shows the resulting fractional rms amplitude of the continuum and QPO components during the first outburst. The continuum amplitude follows the trend described for Figure 11. The QPO amplitude varies from 3% to 13%. As the 10–20 keV flux falls, the ratio of the QPO amplitude to the continuum amplitude increases. For the observation at the peak of the 2–5 keV flux, we have only an upper limit for the continuum rms, which is below the measured QPO amplitude. The power spectrum for this observation is shown in Figure 14.

In Figure 15 we show the frequency evolution of the QPO. The frequency gradually increases during the early stages of the outburst, and around day 60 it exhibits a jump, which coincides with the knee in the flux seen in Figure 2. After that the QPO frequency rises more rapidly, following a different logarithmic trend. The last two frequency measurements were during the state transition episode of the outburst.

4. DISCUSSION

In the course of its X-ray activity, XTE J1908+094 proceeds through a series of X-ray states characteristic of black hole binaries, which we discuss using the terminology proposed by McClintock & Remillard (2004). The discovery outburst begins in the low/hard state, which lasted until about day 87. The source then enters an intermediate state during which the 2–5 keV flux peaks. This ends near day 90 when the source enters the thermal-dominant (high/soft) state, which persists until day 143, just before the secondary peak, where the source enters an intermediate state and then after day 149

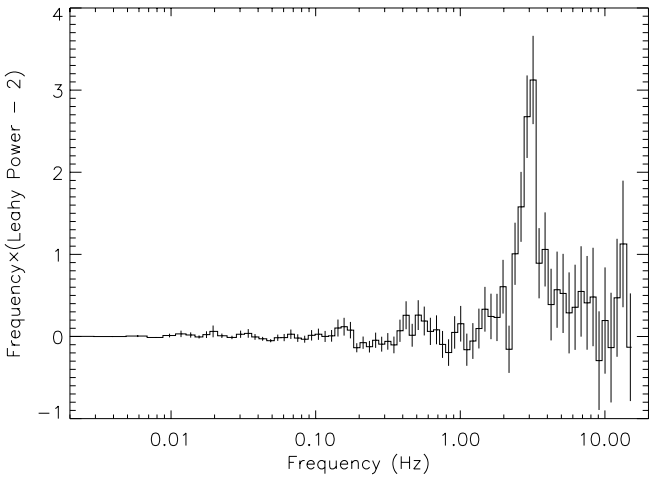

FIG. 14.—Power spectrum from an observation at the peak of the 2–5 keV flux (day 90).

returns to the low/hard state. The remaining observations (in 1.5–12 keV) up to the peak of the second outburst show the source in the low/hard state (see Fig. 1). The one observation following the second outburst peak is consistent with the thermal-dominant state.

In the low/hard state the energy spectra are dominated by a hard power-law component and the power spectra by strong band-limited noise. During the low/hard state at the onset of the first outburst, the index of the power-law spectra began at $\Gamma = 1.4$ and then gradually softened to $\Gamma = 1.7$. The power spectra show band-limited noise with an rms amplitude that began near $r = 30\%$ and gradually fell to $r = 22\%$. In addition, there was a QPO with rms amplitude varying from 3% to 13%, which rose in frequency from 0.5 to 2.2 Hz. In the second interval of the low/hard state (days 149–295) the flux is lower, and the behavior of the power-law index is more complex. Because of the low flux, we could not make significant power-spectral measurements.

Outburst onsets in the low/hard state have been seen in a number of X-ray novae. Brocksopp et al. (2002) tabulate 13 sources with outbursts that began in the low/hard state, five of which never left this state. Strong low-frequency QPOs with rising frequencies are common in these low/hard state onsets and have been seen for GRO J0422+32 (van der Hooft et al. 1999), GRO J1719−24 (van der Hooft et al. 1996), XTE J1550−564 (Finger et al. 1998; Cui et al. 1999), 4U 1630−472 (Dieters et al. 2000), XTE J1859+226 (Markwardt et al. 1999), and XTE J1118+480 (Wood et al. 2000), among others.

Hard X-ray and gamma-ray observations have shown that in the low/hard state the power-law spectra break in the 100 keV range (Grove et al. 1998). In Figure 16 we show our spectral fit for the PCA data on day 64 along with the spectral fit for *BeppoSAX* PDA data from days 62 to 65 (MJD 52,342–52,345) (in't Zand et al. 2002). We notice a break near 50 keV. The flux in the 30–250 keV range is 3.2×10^{-9} ergs cm^{-2} s^{-1}, which surpasses the flux in the 2.5–25 keV range of 2.63×10^{-9} ergs cm^{-2} s^{-1}.

The low/hard state is also associated with radio emission. Flat-spectrum radio emission, associated with compact jets, is consistently observed during the low/hard state of X-ray novae (Fender 2004). Indeed, during the onset of the first XTE J1908+094 outburst, Very Large Array observations (on days 74–75) led to the discovery of a radio counterpart to XTE J1908+094, with a flux of 0.85 mJy at 8.6 GHz (Rupen et al. 2002a). This was detected in additional observations until day 127 (Rupen et al. 2002b).

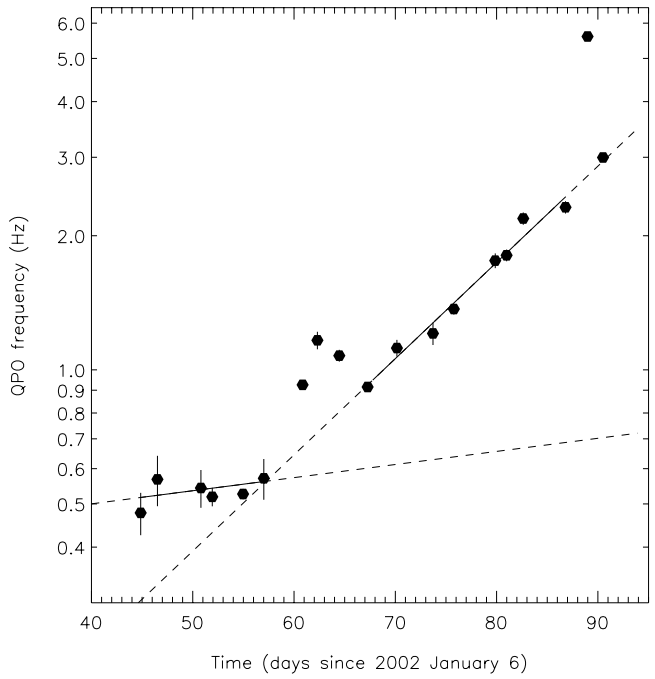

FIG. 15.—Variations in QPO frequency with time. The solid lines indicate the intervals over which the logarithmic-linear fits were performed. The dashed lines are the extrapolations of each fit.

Figure 17 shows the X-ray flux, power-law index, and variability amplitude evolution during the transition interval between the low/hard and thermal-dominant state. This intermediate state begins near day 67, when the power-law flux begins to drop, the power-law component begins to rapidly soften, and the disk blackbody flux begins to rise, and the flux variability begins to fall. The rise of the disk blackbody flux occurs in 4 days, but the fall of the power-law flux takes 15 days to complete. *BeppoSAX* MECS observations covering day 66.4–67.8 (MJD 52,366.4–52,367.8) show the onset of this transition (in't Zand et al. 2002).

In this transition, the total flux in 2.5–25 keV band consistently falls. However, a significant fraction of the disk blackbody flux is below this energy range. From our spectral fits we find that the total integrated flux of this thermal component rises to $\sim 7 \times 10^{-9}$ ergs cm^{-2} s^{-1}, implying that the bolometric flux may be constant or rising.

After day 90 the source is in the thermal-dominant state, with thermal disk flux dominating the spectrum, and low variability. The disk blackbody normalizations average about 40, which is consistent with the inner disk being at the radius of the innermost stable circular orbit if

$$(M/M_{\odot}) D_{10\ \mathrm{kpc}}^{-1} \cos^{1/2}\theta \approx 4.5, \qquad (2)$$

where M is the black hole mass, $D_{10\ \mathrm{kpc}}$ is the source distance in units of 10 kpc, and θ is the disk inclination to the line of sight. Note here that for any value of disk inclination angle, the mass of the central object is in the range of a black hole, if the source distance is of the order of 10 kpc.

During this thermal-dominant state, the flux steadily falls. This mainly occurs as a result of the temperature decreasing. The thermal-dominant state ends on day 149, when a transition begins back to the low/hard state.

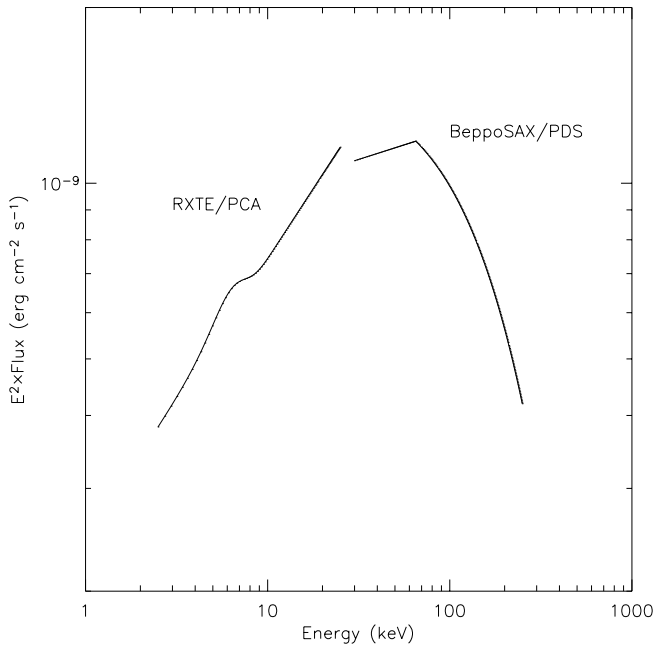

FIG. 16.—*RXTE* PCA spectral fit for day 64 shown together with the *BeppoSAX* PDA spectral fit for days 63–65 from in't Zand et al. (2002).

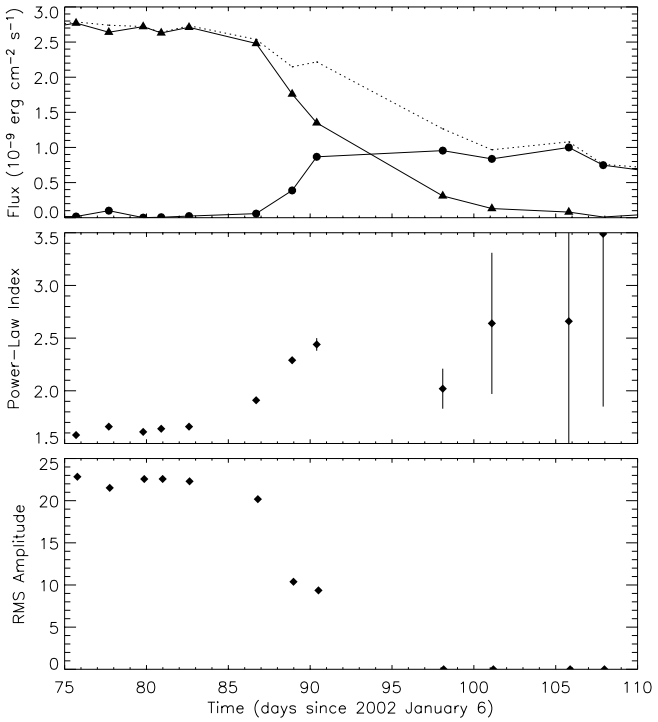

FIG. 17.—Flux, power-law index, and variability evolution during the intermediate state. *Top*: 2.5–25 keV flux for the power law (*filled triangles*), the disk blackbody component (*filled circles*), and their sum (*dashed line*). *Middle*: Power-law index. *Bottom*: Variability amplitude.

In the transition from the low/hard state to the thermal-dominant state starting day 87, the disk blackbody normalization begins near 15 and rises, implying an increasing inner-disk radius. The opposite occurs on the transition back to the low/hard state. This is counter to the expectation that the inner-disk radius is large during the low/hard state and near the innermost stable orbit in the thermal-dominant state (e.g., Esin et al. 1997). This rise and fall may be due to systematic problems with our spectral fits: we detect only the high-energy tail of the thermal spectrum. In fits where the column density, disk temperature, and flux are all free to vary, these parameters are therefore highly coupled. By fixing the column density to the value found with the *BeppoSAX* data, we have reduced this coupling but could be biasing the solution.

There is a strong correlation between the flux associated with the broad-line feature and that of the power-law component during the early stages of the first outburst episode. One possible interpretation of this feature is that it is the fluorescent Fe Kα emission produced by the reprocessing of the hard X-ray photons by cooler material close to the central object. The line centroid energies were somewhat lower than what is expected for neutral iron (6.4 keV). This may suggest that what we observe is primarily the red wing of Doppler-shifted neutral Fe Kα in a Keplerian accretion. This was also seen in 4U 1630−47 (Cui et al. 2000) and in XTE J1748−288 (Miller et al. 2001).

Esin et al. (1997) have presented a model to explain the states of X-ray novae. In the quiescent and low/hard state a thin accretion disk is present but truncated at a large inner radius. Within this radius there is an advection-dominated accretion flow (ADAF), which is a hot and radiatively inefficient flow where most of the thermal energy generated is advected onto the black hole rather then being radiated. Above the accretion disk is a hot corona, which is a continuation of the advection-dominated flow, which produces a power-law spectral component in the low/hard state by Comptonization.

This model does not incorporate the jets, which are responsible for the radio emission now known to be associated with the low/hard state. Markoff et al. (2001) have proposed that these jets also produce the power-law component via synchrotron radiation. In their model a standard accretion disk transitions at an inner radius of $\sim 10^3$ km to a hot ADAF-like flow that feeds the jet. The hard X-rays are synchrotron radiation produced in a shock acceleration region some 10^3 km above the disk plane. The radio emission is from beyond this region.

While providing successful fits of a multiwavelength spectrum, neither of these models yet consider dynamical changes in the flow or attempt to explain the power spectra seen in the different states. The high amplitude variability seen in the low/hard state requires changes in emissivity that are spatially coherent over most of the emission region. It is tempting to associate the QPOs seen in the low/hard state with the Keplerian frequency at the inner edge of the thin accretion disk. Yet while this is plausible in the low/hard state, the QPO in XTE J1908+094 persists into the intermediate state, where the inner-disk radius inferred from spectral fits imply frequencies much larger than those observed.

We thank the anonymous referee for helpful suggestions. E. G., M. H. F., C. K., and P. M. W. acknowledge support from NASA grant NAG5-3370.

REFERENCES

Brocksopp, C., et al. 2002, MNRAS, 331, 765
Cannizzo, J. K. 1993, ApJ, 419, 318
Chaty, S., Mignani, R. P., & Israel, G. L. 2002, MNRAS, 337, L23
Chen, W., Shrader, C. R., & Livio, M. 1997, ApJ, 491, 312
Cui, W., Chen, W., & Zhang, S. N. 2000, ApJ, 529, 952
Cui, W., Zhang, S. N., Chen, W., & Morgan, E. H. 1999, ApJ, 512, L43

Dieters, S. W., et al. 2000, ApJ, 538, 307
Dubus, G., Hameury, J.-M., & Lasota, J.-P. 2001, A&A, 373, 251
Esin, A. A., McClintock, J. E., & Narayan, R. 1997, ApJ, 489, 865
Fender, R. 2004, in Compact Stellar X-Ray Sources, ed. W. H. G. Lewin & M. van der Klis (Cambridge: Cambridge Univ. Press), in press (astro-ph/0303339)
Finger, M. H., Dieters, S. W., & Wilson, R. B. 1998, IAU Circ., 7010, 1
Garnavich, P., Quinn, J., & Callanan, P. 2002, IAU Circ., 7877, 4
Grove, J. E., et al. 1998, ApJ, 500, 899
Homan, J., et al. 2001, ApJS, 132, 377
Hulleman, F., et al. 2001, ApJ, 563, L49
in't Zand, J. J. M., Miller, J. M., Oosterbroek, T., & Parmar, A. N. 2002, A&A, 394, 553
Markoff, S., Falcke, H, & Fender, R. 2001, A&A, 372, L25
Markwardt, C. B., Focke, W. B., Swank, J. H., & Taam, R. E. 1999, BAAS, 31, 1555
McClintock, J. E., & Remillard, R. A. 2004, in Compact Stellar X-Ray Sources, ed. W. H. G. Lewin & M. van der Klis (Cambridge: Cambridge Univ. Press), in press (astro-ph/0306213)
Miller, J. M., et al. 2001, ApJ, 546, 1055
Mitsuda, K., et al. 1984, PASJ, 36, 741
Rupen, M. P., Dhawan, V., & Mioduszewski, A. J. 2002a, IAU Circ., 7874, 1
Rupen, M. P., Mioduszewski, A. J., & Dhawan, V. 2002b, IAU Circ., 8029, 2
Tanaka, Y., & Lewin, W. H. G. 1995, in X-Ray Binaries, ed. W. H. G. Lewin, J. van Paradijs, & E. P. J. van den Heuvel (Cambridge: Cambridge Univ. Press), 126
Valinia, A., & Marshall, F. E. 1998, ApJ, 505, 134
van der Hooft, F., et al. 1996, A&AS, 120, 141
———. 1999, ApJ, 513, 477
Wood, K. S., et al. 2000, ApJ, 544, L45
Woods, P. M., et al. 2002, IAU Circ., 7856, 1